IEEE Access
Multidisciplinary | Rapid Review | Open Access Journal

Received December 31, 2020, accepted January 21, 2021, date of publication January 26, 2021, date of current version February 9, 2021.

Digital Object Identifier 10.1109/ACCESS.2021.3054743

A Novel Approach of Diabetic Retinopathy Early Detection Based on Multifractal Geometry Analysis for OCTA Macular Images Using Support Vector Machine

MOHAMED M. ABDELSALAM[1] AND M. A. ZAHRAN[2]
[1]Department of Computer Engineering and Control Systems, Faculty of Engineering, Mansoura University, Mansoura 36511, Egypt
[2]Theoretical Physics Group, Department of Physics, Faculty of Science, Mansoura University, Mansoura 36511, Egypt

Corresponding author: Mohamed M. Abdelsalam (mohmoawed@yahoo.com)

ABSTRACT Diabetic Retinopathy (DR) is a complication of diabetes that affects the eyes. It is caused by blood vessel damage of the light-sensitive tissue at the back of the retina. Neovascularization are emerged and the small blood vessels are blocked. The prevention or delaying vision loss can be obtained by DR early detection. The retinal microvascular network as a biological system has its own multifractal features as generalized dimensions, lacunarity and singularity spectrum. In this study, a novel approach for DR early detection based on the multifractal geometry has been proposed in some details. Analyzing the macular optical coherence tomography angiography (OCTA) images for diagnosing early non-proliferative diabetic retinopathy (NPDR). Using a supervised machine learning method as a Support Vector Machine (SVM) algorithm to automate the diagnosis process and improving the resultant accuracy. The classification technique had achieved 98.5 % accuracy. This approach also can classify easily other diabetic retinopathy stages or other retinal diseases, which affect the vessels or neovascularization distribution.

INDEX TERMS Diabetic retinopathy, multifractal, optical coherence tomography angiography, support vector machine.

I. INTRODUCTION

Unfortunately, diabetic retinopathy has no early warning signs. For the patients with the fear of vision loss, DR becomes a frightening prospect. Blood vessel damage in the retina is the main diabetic retinopathy pathophysiology, this may cause exudates, hemorrhages, and swelling of the retina [1]. Tiny blood vessels in the human retina were blocked due to increasing the blood sugar ratio. Therefore, the retina blood vessel suffers from bleeding or fluid leakage. Moreover, new several vascular abnormalities as neovascularization are grown on the retina surface, although, this neovascularization frequently does not function well, as well as cause hemorrhage [2]. Preventing or delaying diabetic related blindness can be achieved by the early detection of DR.

The diagnosing algorithms and procedures may differ according to the imaging techniques. The modern Non-invasive technique that can be used for vessel imaging is Optical Coherence Tomography Angiography (OCTA), which has nowadays the upper hand in the early stages of non-proliferative diabetic retinopathy diagnosis. It has the advantages of detecting the early microaneurysms in the retinal microvascular network [3]–[7].

Machine learning is an application of artificial intelligence (AI). It focuses on the development of computer programs for providing systems with the ability to automatically learn and improve from experience. It became one of the most important methods used in medical diagnose. According to the learning algorithms either supervised or unsupervised algorithms, several DR classification techniques had been used. Application of machine learning in the retina and diabetic retinopathy [8], [9]. Using fundus images, different regions of interest were clustered by using the k-means color compression technique, with segmenting out the diabetic parts, finally uses fuzzy inference system (FIS) as a classifier [10].

Several DR classifier techniques were used. In [11], they used a deep neural network as a supervised segmentation technique for a large data sample. Extracting the features,

The associate editor coordinating the review of this manuscript and approving it for publication was Rajeswari Sundararajan.

which were changed due to the morphological changes as the mean of 10 and 20 intercapillary areas as regions of interest include and exclude the Foveal Avascular Zone (FAZ) region, circularity index, FAZ perimeter, and vascular density [12]. Using fundus retinal dataset images, DR was classified by using a deep learning algorithm [13]–[17]. In [18], Convolutional Neural Networks (CNNs) on color fundus images were used with the aid of pretrained AlexNet and GoogLeNet models using two available datasets. Other CNNs as classification techniques were used in [19]–[22].

Based on the Support Vector Machine algorithm as a classifier, a dual classification approach was proposed. Morphology, intensity and gradient based features of the blood vessels create a 21-D feature set, applying genetic algorithm and SVM [23]. In [24], retinal micro-aneurysms and exudates were detected for automatic screening of DR using SVM and k-Nearest Neighbors algorithm (KNN) classifier. Twin support vector machines (TWSVMs) were used for DR detection. The authors used digital fundus images which are fed to the TWSVMs [25]. In [26], they proposed a computer-aided diagnosis (CAD) system for detecting early-stage DR using OCTA images. They extracted vessel density, blood vessel caliber, and width of the FAZ from superficial and deep retinal OCTA. Using SVM with the radial basis function (RBF) kernel as a classifier. The retinal blood vessels structured were segmented from fundus images in [27], a Deep learning- based SVM segmented technique was used for the recognition of both the non-blood and tiny blood vessel pixels. The detailed information about the retinal blood vessels in the final resultant images enable the ophthalmologists in the analyzing and diagnosing severity level.

As a matter of fact, the branching pattern like for example retinal blood vessel matches randomly. The random fractal is designed as a geometrical pattern whose parts resemble in a statistical sense the whole, i.e., statistical self-similar structure. Generally speaking, fractal geometry describes with appreciation success many parts of biological systems that possess strong irregularities where Euclidean geometry failed. Fractals are adequate to characterize many complex physical and biological structures, which cannot display a single length-scale, i.e., self-invariant.

Thus, by using fractal analysis one can find many ways to quantify and measure things that were traditionally meaningless and impossible to measure. Consequently, modeled fractals could be applied successfully in medical digital images, electrochemical patterns, and circulation rhythms. For instance, one of the fractal examples is the cardiovascular system with the regular beating of the human heart. Also, an example of a multifractal pattern is the retinal blood vessel network, which means, it has different fractal properties for their different regions. So, a hierarchy of exponents rather than a single fractal dimension can characterize them.

In essence, one of the most important parameters, which can be used to classify multifractal structures, denoted lacunarity. The lacunarity describes the gaps sizes distribution of an object throughout an image. In fact, lacunarity plays a vital role to identify different structures that may have the same fractal dimension [28]. For example in recent studies [29] have considered the lacunarity for identifying retinal artery and vein blockage that have used for diagnosing amblyopia eyes. In summary, multifractal patterns as the retinal blood vascular network have different regions with different fractal properties, a discrete spectrum of exponents can be used rather than a single-length scale. As is well known, modeling biological systems represent a significant take off both systems biological and medical images.

Multifractal analysis attracted the attention of many researchers in the field of medical diagnosis. In [30], the retinal microvascular networks morphological changes were characterized by diabetic retinopathy progression stages. Microvascular network in high-resolution fundus photography were segmented to a high number of branching generations followed by fractal analysis parameterization. In another study [31], a relationship was established between the fractal dimension (FD), the macular circulation, and the morphology of the FAZ in patients with type 2 Diabetes Mellitus. Fractal dimensional analysis was used for analyzing the retinal vascular disease burden in eyes with diabetic retinopathy using OCTA. With a conclusion that FD for control ayes was significantly higher than diabetic eyes for the superficial and deep capillary plexuses [32]. In [33], new methods for feature extraction from multifractal spectra of retinal vessels were used for diabetic retinopathy classification.

Consequently, although, fractal geometry helped the researchers in measuring the irregularity and complexity of the anatomical structures in the medical images, it can not alone give a numerical decision for the diagnosing of medical image. Hence, several researches used the fractal dimension for observing the differences between the DR stages.

Therefore, the objective of this study is to analyze the macular vascular network using OCTA images by multifractal geometry for normal and NPDR early stages. Use the different generalized dimensions, lacunarity and singularity spectrum characteristics to obtain a numerical decision for the DR diagnosing by the implementation of the SVM algorithm. The SVM is used to summarize the image-extracted features into a single accurate decision, which is very suitable in terms of statistical analysis and feature minimization. This technique is suitable for automatic assessments without the need for extensive user participation.

The contributions of the research can be summarized as:

(1) Several researches use the retinal fundus images in classifying DR rather than the retinal OCTA images. Although, the retinal blood vessels in the retinal microvascular system can be viewed with detailed information by using OCTA images.

(2) A novel study for the classification of DR using multifractal geometry and lacunarity parameters with the usage of the support vector machine algorithm to obtain an accurate single decision.

(3) Extracting the most features, that are correlated to the retinal morphological changes.
(4) The suggested methodology has achieved 98.5% accuracy.
(5) The suggested classification system can be used easily for DR stages detection like non-proliferative DR (moderate and severe) and Proliferative Diabetic Retinopathy PDR.
(6) In addition, it can be used in diagnosing other retinal diseases, which affect the vessels or neovascularization distribution.

II. MATERIAL AND METHODS

A. RETINAL IMAGES

The used research data were approved and obtained by Ophthalmology Center in Mansoura University-Egypt. This study has 170 eye images that have been analyzed. The subjects divided into 90 healthy eyes and 80 eyes of early DR subjects. The subjects are between 45 and 63 years old. These diabetic retinopathy (DR) subjects or normal eyes have been examined clinically by the retinal specialist.

1) The imaging speed is 100,000 A-scans/sec and 1050 nm wavelength
2) B-scans with a four-repeated sequence of 320 A-scans for each 320 raster positions.
3) En-face acquisition areas with dimensions 3*3 mm, 4.5*4.5 mm, and 6*6 mm.
4) Theoretical acquisition time is 4.1 sec.

This research used an angiographic 3*3 mm image with a quality between 35% and 60%.

B. THE OCTA IMAGE PROCESSING SOFTWARE

The subject images have been processed using a custom program written by MATLAB (Mathworks, MA, USA, v.9.4 for R2018a) for contrast and resolution enhancement of the source image as in Fig.1(a). First, obtain the grayscale matrix for the image pixels. Second, verifying and correcting according to a threshold value for showing the microvascular structure pixels as in Fig.1(b). The threshold value can be investigated according to each image, which depends on the image pixels status as the pixels average gray level, the image contrast, and intensity level. Due to the difficulty of describing the morphological features and structures of the retinal microvascular system, the ''Fraclac'' plugin was used for calculating the multifractal parameters and lacunarity measurement. Then create, train, and test the proposed SVM using a custom MATALB program with the evaluation of the classification procedure.

III. THE STUDY METHODS

A. MULTIFRACTAL GEOMETRY

Most medicine and biology structures as the retinal vascular system have irregular forms and can't be described or fully understand by the traditional calculus methods. Actually, there is no, in general, a biological system has a regular Euclidean dimension; almost their dimensions can be described by fractal dimension.

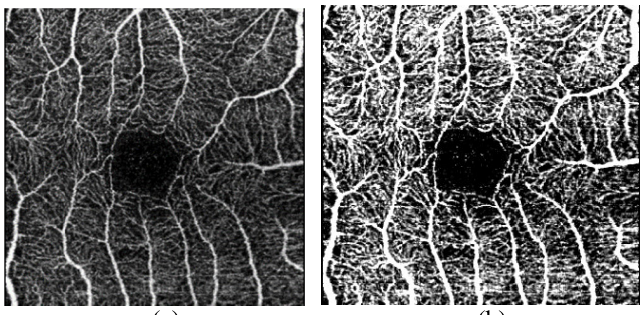

FIGURE 1. The steps of OCTA images processing (a) Source image (b) Improved image contrast.

As is well known, in Euclidean geometry, the line is considered to have one dimension while the rectangle has two dimensions. However, it is easy to infer from Fig.1 that the human retinal vascular network represents a mathematical set that neither a straight line nor two dimensions object, but something between. This means that one has to consult what is called fractal dimension. This concept represents a powerful tool to quantify the complexity, randomness structure, and irregularity especially in medical images as shown in Fig.1.

General speaking, the fractal structure has the following features:

i It has a fine structure at an arbitrarily small scale. It means the fractal parts have the same form or structure as the whole, except that they are at a different scale.
ii It is self-similar, however, not all self-similar objects are fractals.

In concluding the above remarks, fractal objects processes are therefore said to display self-invariant properties, i.e., self-similar or self-affine.

There are many specific definitions of a fractal dimension. A suspect fractal object is examined by the box-counting dimension, the Renyi dimension, the Hausdorff dimension, and the packing dimension [34]–[36]. Indeed the box-counting and correlation are widely used to characterize the fractal structure due to the ease of implementation. In order to obtain the fractal dimension (DF), the method depends on drawing a grid consists of squares with side length ε_1, then determine the number of boxes $N(\varepsilon_1)$ that contain at least one pixel. Next, choose finer and finer grids with side length $\varepsilon_1 < \varepsilon_2 < \varepsilon_3 < \ldots < \varepsilon_m$ and calculate the number of the corresponding boxes as $N(\varepsilon_1), N(\varepsilon_2), N(\varepsilon_3), \ldots N(\varepsilon_m)$ that cover the fractal structure, samples of the covering steps are shown in Fig.2. Therefore, one can get:

$$N(\varepsilon) \sim \varepsilon^{-D_F} \tag{1}$$

where D_F is defined as a fractal dimension.

As a matter of fact, the dimensionality D of space is usually defined as the number of coordinates needed to determine

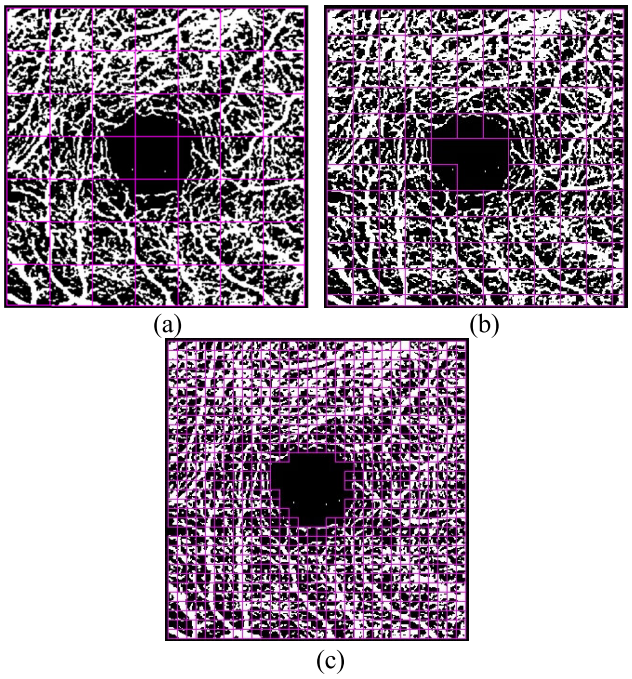

FIGURE 2. Samples of covering grid with different side length.

a unique point in that space. Therefore, the allowed values for D are the non-negative integers i.e., 0,1,2,.... However, the fractal dimension can be redefined so that it still takes on non-negative but real number values.

This is due to the following property that the fractal set is for example a line that can stay written a finite value, but still have an infinite length. This means that it has a complex structure at all lengths of magnifications.

Formula (1) admits in the following form:

$$\ln N(\varepsilon) \sim D_F \ln(\frac{1}{\varepsilon}) \tag{2}$$

Leads to

$$D_F = \lim_{\varepsilon \to 0} \frac{\ln N(\varepsilon)}{\ln(\frac{1}{\varepsilon})} \tag{3}$$

where D_F is defined as fractal dimension, or capacity dimension, or even Mandelbrot box-counting dimension [36] which can be obtained by the asymptotic slope of $N(\varepsilon)$ versus $1/\varepsilon$ in a double logarithmic plot. If the fractal dimension lies somewhere between 0 and 1, this means that the above fractal set is falter than points and thinner than a line. Therefore, such self-similar objects are referred to as fractals since their geometric dimension is often not an integer.

Natural structures have not an exact regular structure as deterministic fractals, they can be considered as non-exact self-similar or have different scales. Noting that, in non-uniform structures with self-similarity properties and rich scaling that can change from point to point, the fractal dimension cannot describe these types of structures. In this case, these structures will be described as ''Multifractals'' rather than fractals. These irregular and multi-scale structures behavior can be found in several biological systems like the nervous system, retina vascular network, circulatory system...etc.

Multifractal structures can be described exactly by employing:

1. The Generalized Dimensions
   a. Box Counting Dimension (D_B),
   b. Information Dimension (D_I),
   c. Correlation Dimension (D_C),
2. The Singularity Spectrum.
3. Lacunarity.

These parameters can be shortly described in the nest section.

IV. THE GENERALIZED DIMENSIONS

Let N_{point} be a large number of points, actually $N_{point} \to \infty$ on a fractal set under consideration. Label ε sized boxes that contain at least one point by i = 1,...,$N_{box}(\varepsilon)$. Assuming that $N_i(\varepsilon)$ be the number of pints in box i. now, one is able to define the generalized dimension as:

$$D_q = \frac{1}{1-q} \lim_{\varepsilon \to 0} \frac{\ln I(q,\varepsilon)}{\ln(\frac{1}{\varepsilon})} \tag{4}$$

where the partition function I(q, ε) is given by

$$I(q,\varepsilon) = \sum_{i=1}^{N_{box}} P_i^q(\varepsilon) \tag{5}$$

With $P_i(\varepsilon) = \frac{N_i(\varepsilon)}{N_{point}}$ is the number of average fractional of points in box i, that represents probabilities with satisfies the normalization condition,

$$\sum_{i=1}^{N_{box}} P_i = \frac{1}{N_{point}} \sum_{i=1}^{N_{box}} N_i(\varepsilon) = \frac{1}{N_{point}} N_{point} = 1 \tag{6}$$

Given a real number q and τ(q) fragmentation ratios for self-similar multifractals, the normalization condition takes the form,

$$\sum_{i=1}^{N_{box}} P_i^q r_i^{\tau(q)} = 1 \tag{7}$$

Noting that, the function τ(q):R→R is a decreasing real analytic function with,

$$\lim_{q \to -\infty} \tau(q) = \infty, \quad \lim_{q \to \infty} \tau(q) = -\infty \tag{8}$$

It is often to denote D_q as Reinyi dimension spectrum and can be put in terms of the scaling function τ(q) as,

$$\tau(q) = D_q(1-q) = \lim_{\varepsilon \to 0} \frac{\ln I(q,\varepsilon)}{\ln(\frac{1}{\varepsilon})} \tag{9}$$

Thus, the generalized form of power law behavior of relation (1) in the limit of $\varepsilon \to 0$ and N→ ∞,

$$Z_q \sim \varepsilon^{D_q(q-1)} \tag{10}$$

It is easy to show that D_q is a non-growing function with q i.e., $D_q \geq D'_q$ if $q \leq q'$. Fig.3 gives the typical behavior of D_q versus q or the generalized dimension spectrum.

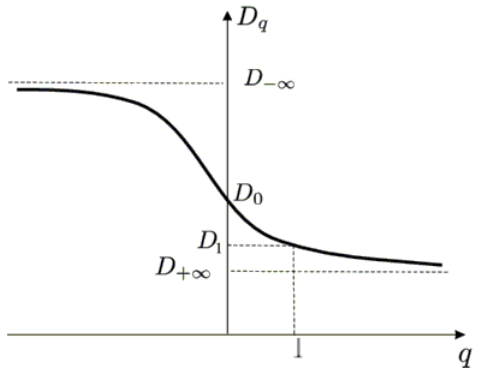

FIGURE 3. The generalized dimensions spectrum.

In self-similar fractal or monofractal, a constant or a flat D_q spectrum with $D_{-\infty} = D_{\infty}$. In the case of D_q is a nonlinear behavior with respect to q, then our fractal set is multifractal i.e., points are non-uniform distributed on the fractal set. Indeed, the bandwidth between $D_{-\infty}$ and D_{∞} as one can infer from Fig.3 measures how large the variation of the fractal dimension is on the multifractal structure.

Practically, there are some important remarks that must be studied in some detail.

A. BOX COUNTING DIMENSION D_B(OR D_0)

When $q = 0$, to obtain D_0 or D_B

$$D_q = \frac{1}{1-q} \lim_{\varepsilon \to 0} \frac{\ln I(q, \varepsilon)}{\ln(\frac{1}{\varepsilon})} \tag{11}$$

Using eq. (6) in above equation, one gets

$$D_q = \frac{1}{1-q} \lim_{\varepsilon \to 0} \frac{\ln \sum_{i=1}^{N_{box}} P_i^q}{\ln(\frac{1}{\varepsilon})} \tag{12}$$

Or,

$$D_q = \frac{1}{1-q} \lim_{\varepsilon \to 0} \frac{\ln N_{box}(\frac{1}{N_{box}})^q}{\ln(\frac{1}{\varepsilon})} \tag{13}$$

This leads to following well-known definition for the generalized fractal definition,

$$D_q = \frac{1}{1-q} \lim_{\varepsilon \to 0} \frac{\ln N_{box}}{\ln(\frac{1}{\varepsilon})} \tag{14}$$

So, the Box counting dimension is the same fractal dimension $D_F = D_0$, taking into account $P_i \sim \frac{1}{N_{box}}$ if $\varepsilon \to 0$. Indeed, the Box counting dimension gives a measure of how the density or self-similarity varies with respect to length.

B. INFORMATION DIMENSION D_I (OR D_1)

When $q = 1$, The partition function can be written as:

$$\ln I(q, \varepsilon) = \ln \sum_{i=1}^{N_{box}} P_i^q(\varepsilon) \tag{15}$$

Employing Taylor expansion admits the following form,

$$\ln I(q, \varepsilon) = (q-1) \ln \sum_{i=1}^{N_{box}} P_i(\varepsilon) \ln P_i(\varepsilon) \tag{16}$$

Therefore, one can get,

$$\lim_{q \to 1} D_q = -\lim_{q \to 1} \frac{1}{1-q} \lim_{\varepsilon \to 0} \frac{\ln I(q, \varepsilon)}{\ln(\frac{1}{\varepsilon})} \tag{17}$$

That leads to,

$$D_I = -\lim_{\varepsilon \to 0} \frac{\sum_{i=1}^{N_{box}} P_i(\varepsilon) \ln P_i(\varepsilon)}{\ln(\frac{1}{\varepsilon})} \tag{18}$$

It worth mention that, the quantity S is known as the Shannon entropy

$$S = -\sum_{i=1}^{N_{box}} P_i(\varepsilon) \ln P_i(\varepsilon) \tag{19}$$

Therefore, the main interesting result is the relation between the information dimension measures the amount of information scales with resolution ε.

$$S(\varepsilon) = -D_I \ln \varepsilon \tag{20}$$

Clearly, above expressions provide that $D_I < D_B$ for non-uniform patterns, but, for uniform patterns, the expression will be $D_I = D_B$. Therefore, the information dimension describes the increasing in the region morphology as $\varepsilon \to 0$.

C. CORRELATION DIMENSION DC (OR D2)

In case of $q = 2$, D_q then denoted the correlation dimension. The partition function can be written as:

$$\ln I(q = 2, \varepsilon) = \ln \sum_{i=1}^{N_{box}} P_i^2(\varepsilon) \tag{21}$$

Then one easily gets,

$$D_c = D_2 = \lim_{\varepsilon \to 0} \frac{\ln I(q = 2, \varepsilon)}{\ln(\frac{1}{\varepsilon})} \tag{22}$$

Noting that in the case of $q > 0$, contribution to $I(q, \varepsilon)$ from regions of high density on the multifractal system is much more compared to low-density regions. That is meant that the quantity D_q with large q is the main feature of high-density clustering regions.

Remarkably, the correlation dimension plays a vital role to classify all multifractal structures especially in the characterizing of the non-uniform point pattern. It represents a good indicator regarding the inhomogeneous pattern distribution of the structure under consideration, i.e. gives a direct relation between two pixels inside a region under study.

The formal dimension definitions for uniform patterns leading to

$$D_C = D_I = D_B \tag{23}$$

In non-uniform distribution, the relation will be

$$D_C < D_I < D_B \tag{24}$$

Therefore, in the human retina, box-counting, information and correlation dimensions are significantly different.

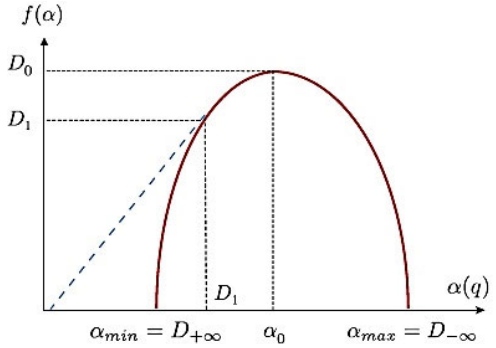

FIGURE 4. The f(α) spectrum.

V. THE SINGULARITY SPECTRUM f(α)

The singularity spectrum $f(\alpha)$ is considered a significant way of describing the multifractal behavior. It shows the distribution of the singularity exponents. It gives complete information about the nonlinearity degree and its nature. The D_q versus $f(\alpha)$ transformation equations can be written as

$$\tau(q) = (1-q)\, D_q \tag{25}$$

By using Legendre Transformation Eq (25) admits,

$$\tau(q) = f(\alpha) - q\alpha \tag{26}$$

where the factor α is based on the real number q, solve the Eq. (26) leads to,

$$\frac{d}{dx}(q\alpha - f(\alpha)) = 0 \tag{27}$$

With known $\tau(q)$, the singularity spectrum can be expressed as

$$f(\alpha(q)) = \tau(q) + q\alpha(q) \tag{28}$$

The value of α gives the information regularity points. Hence, each pixel is characterized by its α value. The singularity spectrum $f(\alpha)$ gives a measure of the heterogeneity degree of regions. The region is considered an homogeneous state if $f(\alpha)$ is close to 1 or 2 as in Euclidean geometry. The broader the $f(\alpha)$ spectrum, the more heterogeneity regions for different α values. The singularity spectrum $f(\alpha)$ is shown in Fig.4.

VI. LACUNARITY MEASUREMENT

According to the previous discussion, the retinal microvascular network can be considered as multifractal structures. The microvascular distribution varies from a subject to the other according to the diabetic stage. So, we need a measure that describes how much space is filled with the object. Mandelbrot [37] introduced ''Lacunarity'' as a measure for describing the sizes of gaps distribution or lacunae surrounding the object within the image.

The lower lacunarity reflects the lower size distribution of gaps ''low degree of gappiness''. In our case, the higher the lacunarity, the higher microvascular sized gaps. Lacunarity can be calculated using the gliding-box algorithm [38].

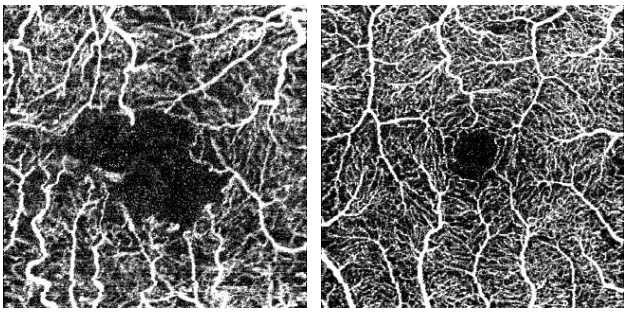

FIGURE 5. Different gaps sizes and distribution (a) Large gaps with different bifurcation microvascular sizes (b) less gaps with less bifurcation microvascular sizes.

Image-J and FracLac plugin can be used to calculate lacunarity ''λ''. Many λ^s can be obtained according to the sampling unit size. The mean lacunarity (or Λ) for all the used sample sizes was expressed as:

$$\Lambda = \frac{\sum(1 + (\sigma/\mu)^2)}{n} \tag{29}$$

where σ is the standard deviation, μ is the mean for pixels per box at this size δ and n is the number of box sizes. Figure 5 shows a comparison of two images that having gaps with different sizes and distribution. The lacunarity measure can be illustrated in Fig.5. Figure 5(a) shows a retinal microvascular network image with large gaps between the vessels and random distribution, as well as the image has different bifurcation blood vessel sizes the lacunarity = 0.389. While in Fig.5(b), the microvascular network has fewer gaps, semi-normal distribution and less bifurcation microvascular sizes with lacunarity = 0.221. Therefore, the lacunarity is considered a good measure for describing the sizes of gaps distribution.

A. CASE STUDY

Let us illustrate the previous concepts by a retinal image example. Figure 6 shows the source OCTA retinal image with its multifractal analysis results. The source image Fig.6 (a) has a moderate resolution with little artifacts. Using a custom-written program in MATLAB software and FracLac plugin based Image-J software, the multifractal analysis results are illustrated in Fig.6 (b) and (c). Figure 6 (b) shows the generalized dimensions of the selected images using the box-counting algorithm. The box-counting dimension D_B = 1.92 rather than 2, which reflects the non-exact self-similarity in the retinal vascular network. The Shannon or Information dimension D_I = 1.88 which means there are some morphological changes in the retinal vascular network in the image zones which may be due to microaneurysms and neovascularization in DR stages. The correlation dimension D_C = 1.86 which reflects the degree of correlation between pair of pixels in each box. Therefore, here the pixels have not a complete correlation, which means there are little gaps between the pair of pixels.

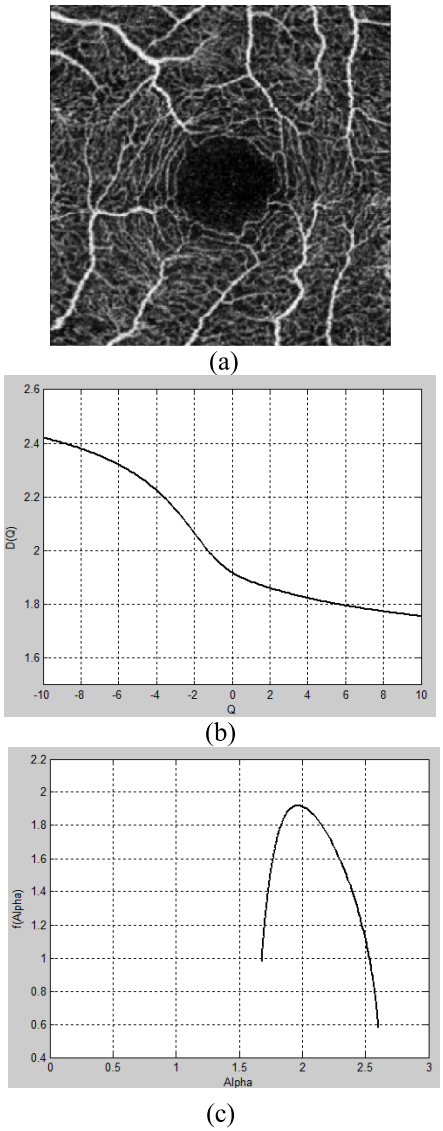

FIGURE 6. Sample image with multifractal analysis results. (a) The source image (b) Generalized dimension curve (c) The singularity spectrum.

Figure 6(c) shows the f(α) singularity spectrum. The f(α) spectrum has a wide range of variability. It starting at f(α) = 0.971 then it increased to 1.92, then reduced again to 0.575. This wide range of variability (broader spectrum) means that the image has different heterogeneity zones.

Therefore, by using multifractal geometry, we can extract particular image regions' features that usually invisible. These analyses are very important and useful in medical diagnosis applications. The multifractal applications in medicine seem to be very promising tools.

VII. SUPPORT VECTOR MACHINE ALGORITHM IN BRIEF

A support vector machine is a supervised machine learning algorithm that can be used in classification and regression problems. The main idea of SVM is: The algorithm creates a line or a hyperplane, which separates the data into classes.

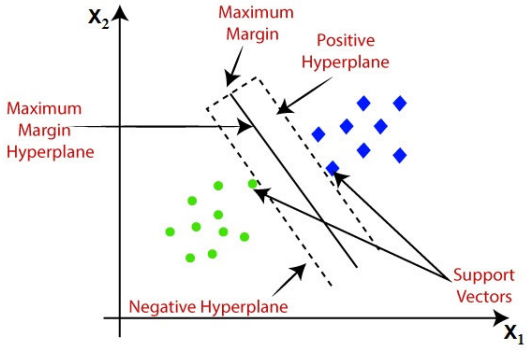

FIGURE 7. Support vector machine algorithm.

At first, the data are plotted in n-dimension axes; hence n is the number of classification features. Then, draw a hyperplane or a straight line to separate the input data. The data points nearest to the hyperplane are called support vectors. This hyperplane is the decision boundary, where any data point that falls to one side of it, the data will be classified according to the location side.

For training dataset:

$$(x_1, y_1), ..., (x_n, y_n), x_i \in R^d \text{ and } y_i \in (-1, +1) \quad (30)$$

where x_i is the feature vector and y_i is the class label of a training item i.

For a two-class classification system, the hyperplane can be written as:

$$wx^T + b = 0 \quad (31)$$

where x is the input feature vector, w is the weight vector, and b is the bias.

The objective of the training procedure of SVM is to find the w and b to satisfy the following inequalities for all elements of the training set and maximizes the margin:

$$\begin{cases} wx_i^T + b \geq 1 & \text{if } y_i = 1 \\ wx_i^T + b \leq -1 & \text{if } y_i = -1 \end{cases} \quad (32)$$

The SVM algorithm for two classes is shown in Fig.7.

Several hyperplanes can be drawn for separating the data points, but the best hyperplane whose distance to the nearest data element is the largest (Maximum Margin) [39]. The SVM algorithm is implemented in practice using a kernel. A kernel transforms an input data space into the required form [40]. The Kernel type depends on the data point's separation type, which is shown in Table 1.

SVM has several advantages as:1) it is very efficient even with high dimensional data 2) less training time, 3) it can perform well even the number of features is more than the data rows, 4) Used for classification and regression.

Although SVM has limitations as: 1) choose an optimal kernel for SVM for best classification 2) in case of the large number of features, an over-fitting may

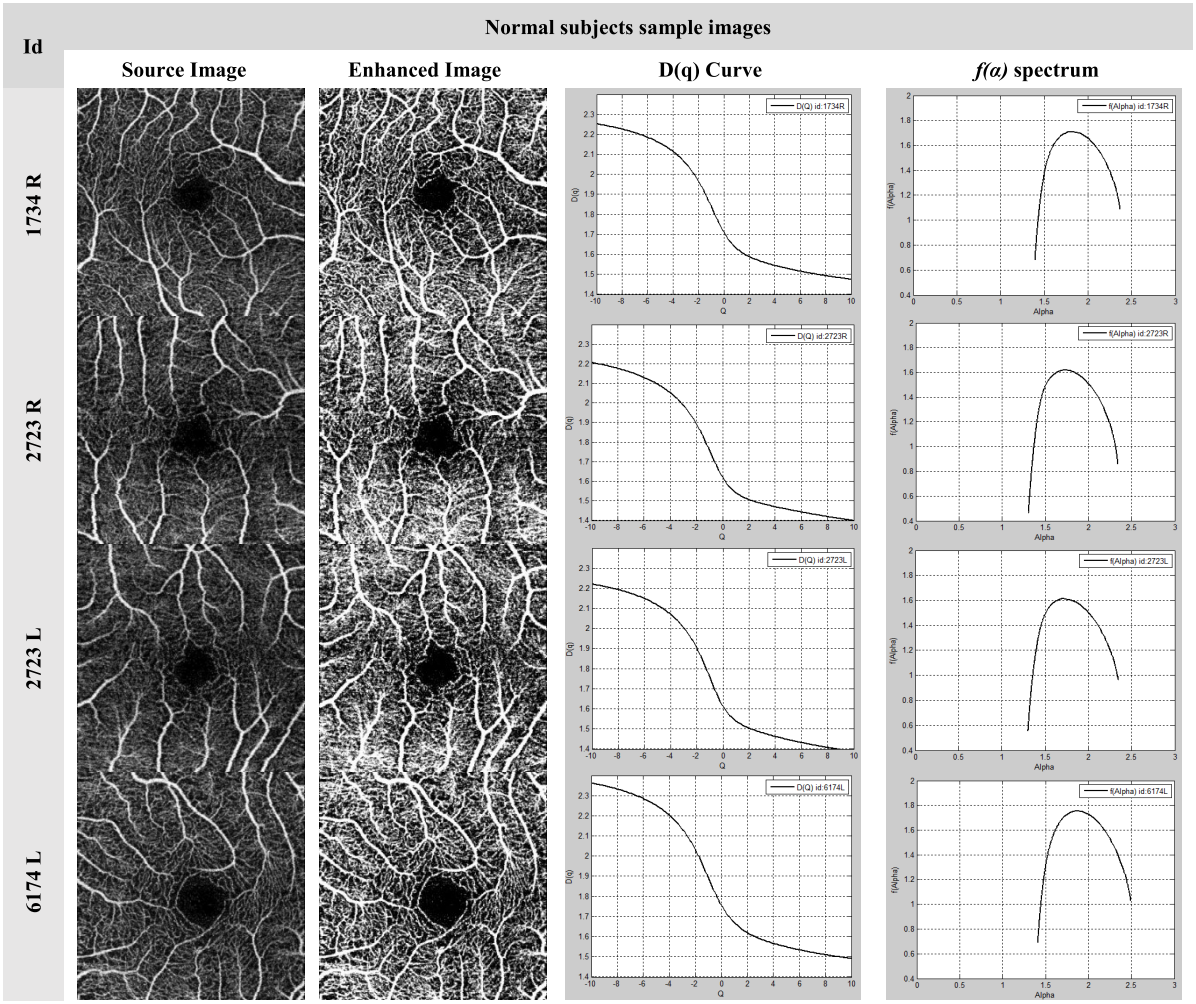

FIGURE 8. The Normal subject images.

TABLE 1. SVM kernel.

Type of SVM	Kernel
Linear	$K(x_1, x_2) = {x_1}^T x_2$
Polynomial	$K(x_1, x_2) = ({x_1}^T x_2 + 1)^\rho$
Radial Basis Function (RBF)	$K(x_1, x_2) = \exp(-\frac{\|x_1 - x_2\|^2}{2\sigma^2})$

ρ: the polynomial order, σ: the Kernel width

occur. 3) Long training time for large datasets [41]. SVM attracted the researcher's attention for many applications as seismic liquefaction potential [42]–[46], data classification [47]–[50], texture classification [51],[52], face and speech recognition [53]–[54], [55], cancer diagnosis and prognosis [56],[57], protein fold and remote homology detection [58]–[61] and others [62]–[65].

In this study, the classification procedure depends on the usage of a support vector machine, which can be a useful classifier tool, especially in small and non-singularity datasets. The training procedure depends on using the seven extracted features as the training datasets. The extracted features are distinct between the two classified stages, which are a good choice for the classification process. The training datasets are in numerical format rather than a complete image, so no need for extra datasets. The proposed classification system can be described as:

1. Extracting the most seven features, which is related to the multifractal analysis and correlated to the retinal morphological changes according to DR stages. The features are:
   a. The α at the maximum of the singularity spectrum $f(\alpha)$.
   b. The shift in the singularity spectrum symmetrical axis.
   c. The width of the singularity spectrum (W).
   d. The Lacunarity (Λ).
   e. The Box counting dimension D_B.
   f. The Information Dimension D_I.
   g. The Correlation Dimension D_C.

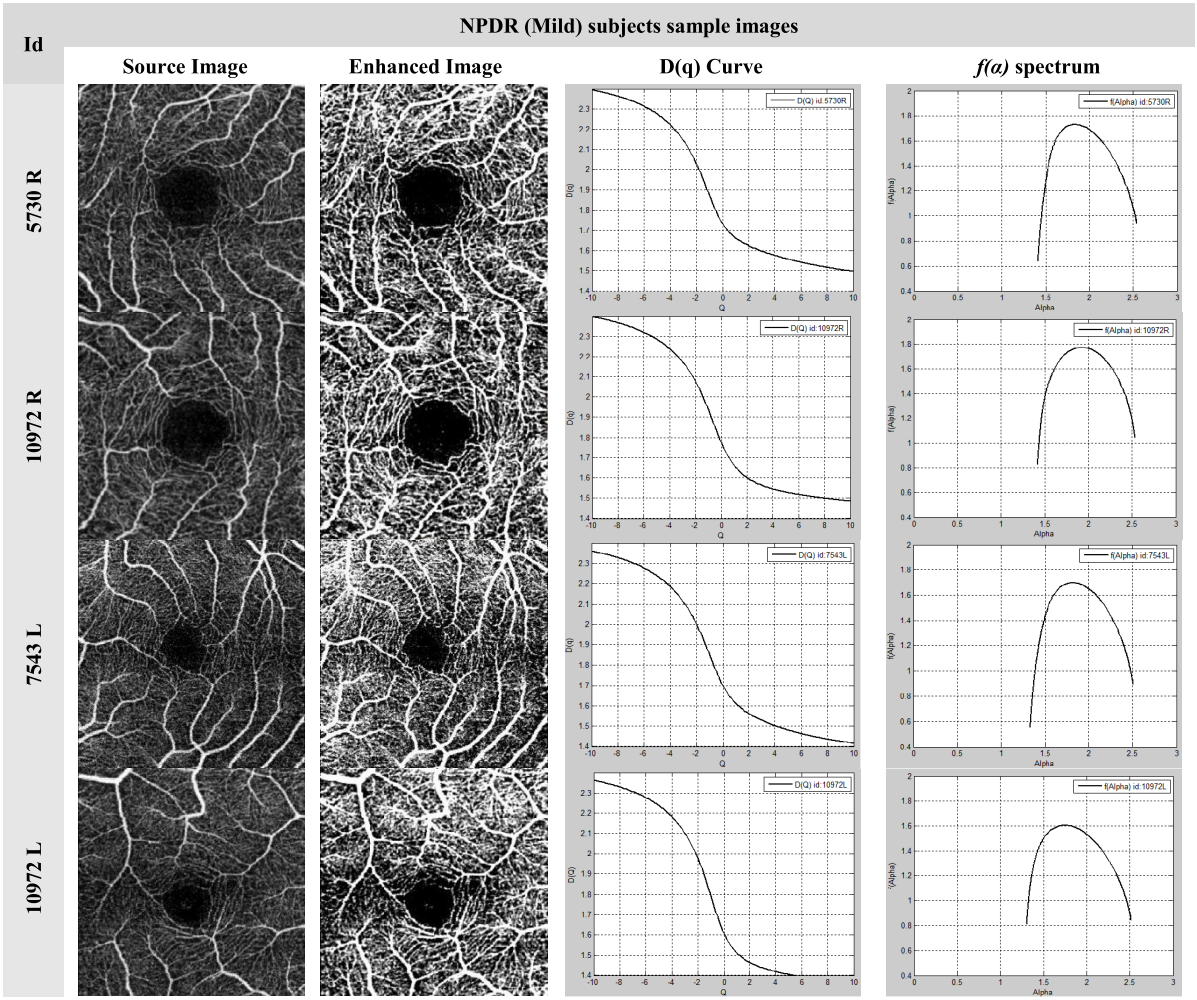

FIGURE 9. The NPDR subject images.

2. These generalized dimensions describe the self-similarity, morphological characteristic and pixels correlation of the retinal vascular images.
3. The singularity spectrum description features for the retinal image heterogeneity characteristics with lacunarity.
4. The objective is to classify the input data images to two-class normal and NPDR.

TABLE 2. The subjects demographic characteristics.

Characteristics	Normal (N=90)	Mild NPDR (N=80)	p-value
Age (y) average ± STD	54.6± 7.7	58.56±8.3	0.2268
Female/male (N)	56/34	32/48	0.5179
Laterality (RT/LT)	62/28	29/51	0.1975

VIII. RESULTS

A. DEMOGRAPHIC CHARACTERISTICS

In this study, 170 eye images have been analyzed, 90 images for normal and 80 images for early DR (mild non-proliferative diabetic retinopathy) subjects. Table 2 shows the studied Subjects' demographic characteristics.

Table 2 shows the examined subjects' demographic characteristics. In this study, the statistical metric P-value had been used for assessing the subjects' significance. The data were non-significant, in the case of the P-value ($P > 0.05$). The subjects average ages are 54.6 and 58.56 years for normal and Mild NPDR respectively, which is statistically non-significant with ($P > 0.2268$). The subjects' sex were 88 for Females and 82 for Males, with ($P > 0.5179$). The laterality numbers (RT/LT) were 91/79 with ($P > 0.1975$). Therefore, the subjects under study were statistically non-significant.

B. IMAGE ANALYSIS

Figure 8 shows, four main normal image samples with the following id 1734R, 2723R, 2723L and 6174L respectively,

TABLE 3. The result parameters for the image analysis.

Image		D(Q)			f(α)			Lacunarity
Id	Status	D_B	D_I	D_C	α at max	Spectrum width	symmetric shift	
1734R	N	1.711	1.63	1.589	1.821	0.9728	0.0614	0.2663
2743R	N	1.632	1.562	1.524	1.734	0.991	0.1025	0.2467
2794R	N	1.653	1.58	1.535	1.7453	1.049	0.0412	0.2613
2723R	N	1.62	1.542	1.51	1.731	1.031	0.0945	0.2282
6174R	N	1.679	1.61	1.578	1.783	0.981	0.1005	0.2582
2723L	N	1.613	1.54	1.504	1.722	1.035	0.1005	0.2574
2794L	N	1.543	1.468	1.438	1.661	1.078	0.173	0.2537
5407L	N	1.544	1.454	1.414	1.672	1.014	0.091	0.2672
5721L	N	1.651	1.552	1.5	1.787	1.171	0.0245	0.2381
6174L	N	1.757	1.67	1.62	1.87	1.082	0.083	0.2497
47R	NPDR	1.805	1.734	1.695	1.902	1.084	0.138	0.3306
5729R	NPDR	1.66	1.587	1.551	1.763	1.173	0.1805	0.2754
5730R	NPDR	1.733	1.663	1.625	1.836	1.123	0.1365	0.3405
10972R	NPDR	1.776	1.662	1.601	1.924	1.113	0.0515	0.2694
11163R	NPDR	1.641	1.542	1.494	1.775	1.279	0.1455	0.2886
7912L	NPDR	1.766	1.7	1.661	1.856	1.108	0.09	0.2804
7536L	NPDR	1.75	1.639	1.577	1.9	1.357	0.1025	0.2921
7543L	NPDR	1.7	1.612	1.563	1.821	1.171	0.0945	0.2682
10972L	NPDR	1.607	1.511	1.466	1.747	1.203	0.1615	0.2956
2944L	NPDR	1.779	1.747	1.72	1.92	0.928	0.186	0.3489

TABLE 4. The classification data.

Item	Normal	NPDR	Total
Subject Images	90	80	170
Trained Images	60	43	103
Tested Subjects	30	37	67
Correctly classified	30	36	66
Incorrectly classified	0	1	1
Classification Accuracy	100%	97.3%	98.5%

with their processed images and multifractal analysis results (generalized dimensions and singularity spectrum). Figure 9 is the same as Fig.8, except it is for NPDR images with the following id 5730R, 10972R, 7543L and 10972L respectively.

The retinal microvascular network images had been processed and analyzed using the multifractal geometry, in order to extract the parameters that describe the gaps distribution, vessel heterogeneity and the blood vessels' random distribution. The selected parameters are listed before.

Table 3 shows the seven parameters for 20 sample images. Ten sample images for normal subjects and 10 sample images for NPDR subjects.

In this study, the classification had been done by using an SVM classifier with RBF kernel. The multifractal parameters that resulted from the studied images were the SVM features. In the training step, the datasets were 113 images, while new 67 images were used in the testing step. The detailed numbers are shown in Table 4.

IX. DISCUSSION

Figures 8 to 10 show the generalized dimensions for both normal and pathological cases. It is clear that the

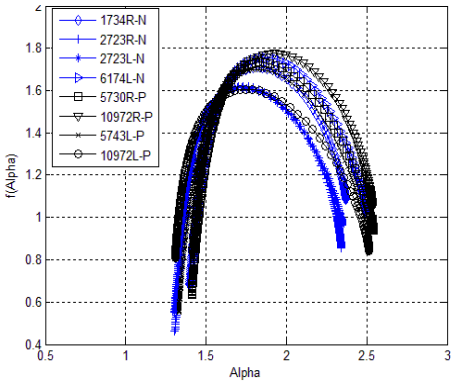

FIGURE 10. Sampled images f(α) spectrum.

pathological (NPDR) curves have slight changes, which cannot enable to reach an accurate decision. It is noticeable that the f(α) spectrum in NPDR cases shifted slightly to the right and exceed $\alpha = 2.5$ with as shown in Fig.8 with a slight increase in the spectrum curves width and have average symmetrical shift 0.185. While in normal cases the value of α didn't exceed 2.5 with less spectrum width and less symmetrical shift 0.078 which means it is more symmetrical than the NPDR cases. So, it is a good metric that can be used in the classification process. Therefore, to accurately classify the resulted data, it is necessary to have complete information about the multifractal spectra. These parameter sets lead to decision-making in NPDR and normal subjects' classification.

As illustrated in Fig.11, the generalized dimensions for both normal and NPDR subjects Fig.11 (a), (b) and (c) satisfy the inequality $D_B \geq D_I \geq D_C$, which confirms that the studied images have multifractal nature. The average generalized

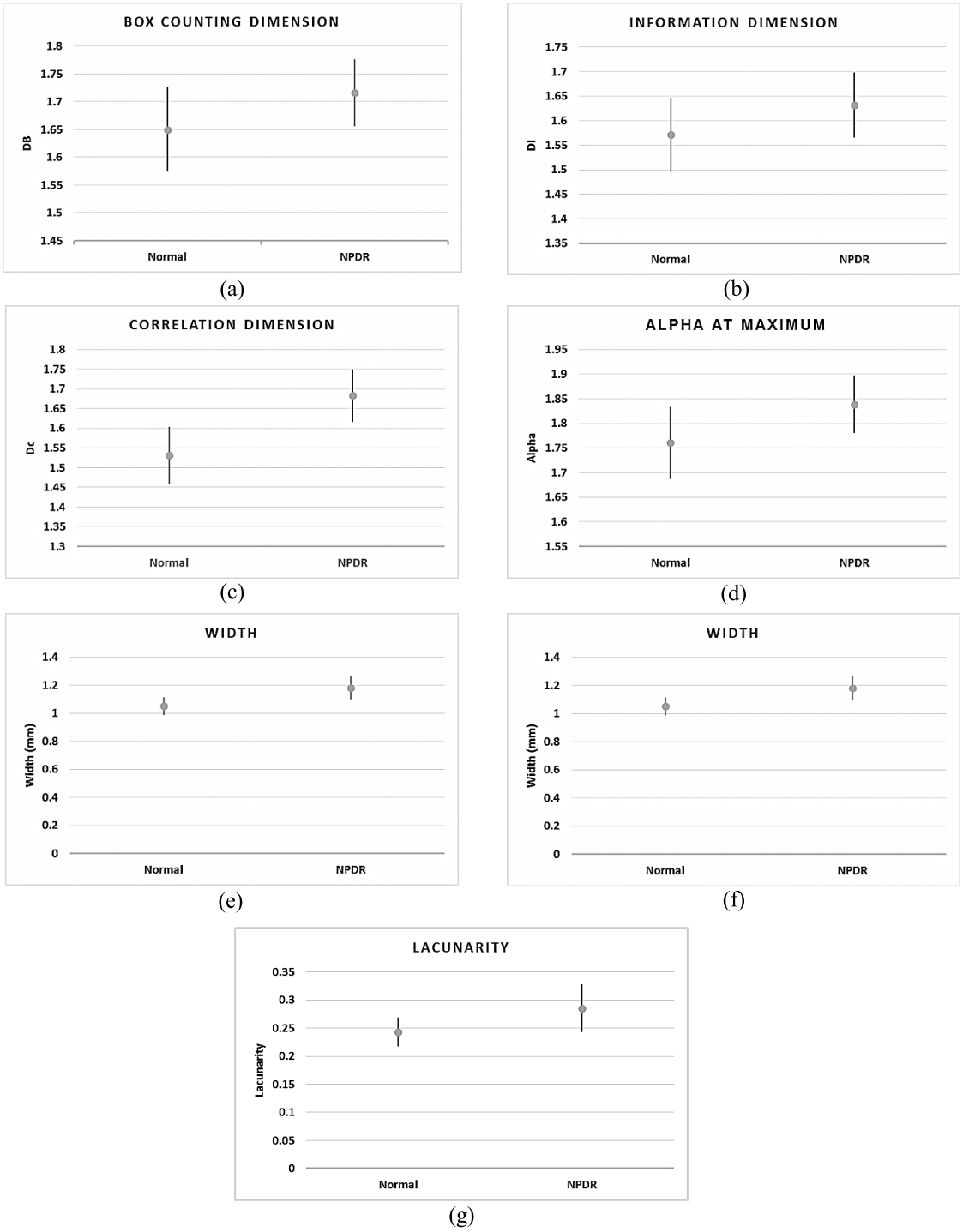

FIGURE 11. The statistical representation of the extracted.

dimensions in normal subjects are less than their counterparts in NPDR subjects. This is due to increasing the number of occupied pixels (density) this arising from the new microaneurysms in NPDR subjects. The NPDR cases have a broader f(α) spectrum with slight shift due to more heterogeneity in the vascular network images, this can be illustrated in Fig.10 and Fig.11 (d), (e) and (f). The mean of the lacunarity in normal subjects is 0.243 with little increase in NPDR to reach 0.285, this is back to the sizes of the new gaps due to the blocked blood vessel.

To ensure the proposed classification system quality, classification accuracy, sensitivity, specificity, confusion matrix, and precision were used. After the SVM training, 67 new subject eyes were used for testing, 30 images for normal eyes

TABLE 5. Confusion matrix.

Actual status	Classified Healthy	Classified Diabetic
Normal (30)	30 TP (True Positive)	0 FN (False negative)
Mild NPDR (37)	1 FP (False Positive)	36 TN (True Negative)

TABLE 6. Sensitivity, specificity and precision parameters.

Sensitivity (%)	100
Specificity (%)	97.3
Precision (%)	96.8

and 37 images for NPDR eyes. Table 5 and Table 6 summarize the performance measures.

Where

TP: True Positive, it is the number of normal images that classified correctly.

TN: True Negative, it is the number of NPDR images that classified correctly.

FN: False Negative, it is the number of normal images that classified as NPDR (incorrectly).

FP: False Positive, it is the number of NPDR images that classified as normal (incorrectly).

$$Sensitivity(\%) = \frac{TP}{TP + FN} \times 100 \quad (33)$$

$$Specificity(\%) = \frac{TN}{TN + FP} \times 100 \quad (34)$$

$$Precision(\%) = \frac{TP}{TP + FP} \times 100 \quad (35)$$

From tables 5 and 6, the statistical parameters confirm that the classification accuracy is within 98.5%. The classification system achieves sensitivity with 100%, specificity with 97.3%, and 96.8% in precision. With a low misclassification error 1.5%.

X. COMPARATIVE EVALUATION

In addition to the obtained results, we want to verify the effectiveness of the proposed approach in the classification problem. The performance of the proposed classification method was listed and compared with some previous studies considering the same classification topic. Table 7 shows the comparative evaluation of different studies, the best values are written in bold style.

As illustrated in Table 7, different classification techniques were listed with their performance measures. Two techniques such as Principle Component Analysis (PCA) with firefly [66] and [67] used a deep neural network approach. Two studies based on CNN [13], [68], add two more studies based on Support Vector Machine (SVM) have been included [24], [26]. Another study used K-nearest neighbor (KNN) with Fractal analysis [69]. Accuracy, sensitivity and specificity have been evaluated for all the methods.

TABLE 7. Comparative evaluation techniques.

Methods	*Accuracy*	*Sensitivity*	*Specificity*	*Dataset images*
CNN + Image processing [13]	97%	94%	98%	400
K-nearest neighbor (KNN)+ Fractal analysis [69]	89.17%	-	-	120
Entropy CNN classification [68]	86.1%	73.24%	93.81%	21,123
DNN- Principle component analysis (PCA) - Firefly [66]	97%	92%	95%	1151
(SVM) + Gray-level Co-occurrence Matrix (GLCM) [24]	82%	98%	89%	-
Deep neural network (DNN) [67]	98% (ROC)	90%	96%	294
SVM+ Radial Basis Function (RBF) [26]	94.3%,	97.9%	87.0%	105
Multifractal + SVM (this study)	**98.5%**	**100%**	**97.3%**	**170**

Where ROC : Receiver Operating Characteristic Curve

The proposed multifractal geometry with the SVM algorithm had achieved a classification accuracy of 98.5% with 100% sensitivity and 97.3% for specificity. From the comparative results, the proposed classifier technique gives better results than other methods in the previous studies. The DNN technique [67] achieved a slight decrease in the accuracy (ROC) by 0.5% with lower values in the other performance measures. The studies [24], [26] had achieved decreasing in the sensitivity by 2% and 2.1% respectively, hence our proposed technique has higher accuracy and specificity measures. The study [13] had achieved a slight increase in the specificity by 0.7%, but, with lower accuracy and sensitivity than the proposed classification technique.

Finally, the proposed technique had achieved the best performance measures for diabetic retinopathy early detection. These measures can be enhanced by increasing the training datasets. This technique can be used for the classification of the diabetic retinopathy stages. One of the proposed technique challenges is image quality. The images that have been worked on have a quality between 35% to 65%. If the OCTA image quality below 30% (which may be difficult even for physicians to diagnose), bad extracted features will be obtained.

XI. CONCLUSION

The present work aims to develop a new accurate and efficient algorithm based on the framework of multifractal analysis to

classify and characterize any complex shapes and branching patterns found in physics and biology.

We represent such a simple technique in order to obtain a more accurate human retinal network description instead of a traditional Euclidian study. This study provides us strong evidence that multifractal analysis will play a vital screening tool for retinal diseases early detection. The interest in understanding our study has resulted in the development of a considerable number of graphs to study the parameter α with the variation of entropic function $f(\alpha)$.

Multifractal and Lacunarity enable us to visualize the vascular structure distribution for both normal and NPDR cases. Interestingly, one can infer that there are appreciate differences between both normal and NPDR subjects. In addition, to the above remark, there is also a slight right shift in the singularity spectrum for most NPDR cases, i.e. an obvious broken of symmetries of the curves represent these mentioned cases. On the other hand, in normal cases, there is a symmetrical behavior of entropic function $f(\alpha)$.

In summary, this research work has emphasized the necessity for an automated technique for NPDR retinal image classification. Moreover, this road map reminds us the evaluation of the Skeleton could in principle promising approach to get many fractal features like for instance, information and correlation dimensions in order to have good ideas concerning the existence of gaps and the bifurcation point as well.

In addition, the support vector machine has been employed to the obtained multifractals parameter to give us a computational simple recipe and attains accurate detection concerning early diabetic retinopathy. The proposed technique has achieved an accuracy of 98.7%. It worth mention that, this approach in essence it can be used to classify different diabetic retinopathy stages.

FUTURE WORK

- Design a new GUI application that can extract the selected image features for early detection and diagnosing.
- The detection and extraction of malignant.

REFERENCES

[1] R. Donnelly, "ABC of arterial and venous disease: Vascular complications of diabetes," *BMJ*, vol. 320, no. 7241, pp. 1062–1066, Apr. 2000, doi: 10.1136/bmj.320.7241.1062.

[2] M. Brownlee, "The pathobiology of diabetic complications: A unifying mechanism," *Diabetes*, vol. 54, no. 6, pp. 1615–1625, Jun. 2005, doi: 10.2337/diabetes.54.6.1615.

[3] T. E. D. Carlo, A. Romano, N. K. Waheed, and J. S. Duker, "A review of optical coherence tomography angiography (OCTA)," *Int. J. Retina Vitreous*, vol. 1, no. 1, p. 5, Apr. 2015, doi: 10.1186/s40942-015-0005-8.

[4] R. F. Spaide, J. G. Fujimoto, N. K. Waheed, S. R. Sadda, and G. Staurenghi, "Optical coherence tomography angiography," *Prog. Retinal Eye Res.*, vol. 64, pp. 1–55, May 2018, doi: 10.1016/j.preteyeres.2017.11.003.

[5] R. F. Spaide, J. M. Klancnik, and M. J. Cooney, "Retinal vascular layers imaged by fluorescein angiography and optical coherence tomography angiography," *JAMA Ophthalmol.*, vol. 133, no. 1, p. 45, Jan. 2015, doi: 10.1001/jamaophthalmol.2014.3616.

[6] A. Rabiolo, F. Gelormini, R. Sacconi, M. V. Cicinelli, G. Triolo, P. Bettin, K. Nouri-Mahdavi, F. Bandello, and G. Querques, "Comparison of methods to quantify macular and peripapillary vessel density in optical coherence tomography angiography," *PLoS ONE*, vol. 13, no. 10, Oct. 2018, Art. no. e0205773, doi: 10.1371/journal.pone.0205773.

[7] P. Jirarattanasopa, S. Ooto, A. Tsujikawa, K. Yamashiro, M. Hangai, M. Hirata, A. Matsumoto, and N. Yoshimura, "Assessment of macular choroidal thickness by optical coherence tomography and angiographic changes in central serous chorioretinopathy," *Ophthalmology*, vol. 119, no. 8, pp. 1666–1678, Aug. 2012, doi: 10.1016/j.ophtha.2012.02.021.

[8] A. Kumar, S. Padhy, B. Takkar, and R. Chawla, "Artificial intelligence in diabetic retinopathy: A natural step to the future," *Indian J. Ophthalmol.*, vol. 67, no. 7, p. 1004, 2019, doi: 10.4103/ijo.IJO_1989_18.

[9] U. Schmidt-Erfurth, A. Sadeghipour, B. S. Gerendas, S. M. Waldstein, and H. Bogunovic, "Artificial intelligence in retina," *Prog. Retinal Eye Res.*, vol. 67, pp. 1–29, Nov. 2018, doi: 10.1016/j.preteyeres.2018.07.004.

[10] M. Jahiruzzaman and A. B. M. A. Hossain, "Detection and classification of diabetic retinopathy using K-means clustering and fuzzy logic," in *Proc. 18th Int. Conf. Comput. Inf. Technol. (ICCIT)*, Dec. 2015, pp. 534–538, doi: 10.1109/ICCITechn.2015.7488129.

[11] P. Liskowski and K. Krawiec, "Segmenting retinal blood vessels with_newline deep neural networks," *IEEE Trans. Med. Imag.*, vol. 35, no. 11, pp. 2369–2380, Nov. 2016, doi: 10.1109/TMI.2016.2546227.

[12] M. M. Abdelsalam, "Effective blood vessels reconstruction methodology for early detection and classification of diabetic retinopathy using OCTA images by artificial neural network," *Informat. Med. Unlocked*, vol. 20, 2020, Art. no. 100390, doi: 10.1016/j.imu.2020.100390.

[13] D. J. Hemanth, O. Deperlioglu, and U. Kose, "An enhanced diabetic retinopathy detection and classification approach using deep convolutional neural network," *Neural Comput. Appl.*, vol. 32, no. 3, pp. 707–721, Feb. 2020, doi: 10.1007/s00521-018-03974-0.

[14] Z. Gao, J. Li, J. Guo, Y. Chen, Z. Yi, and J. Zhong, "Diagnosis of diabetic retinopathy using deep neural networks," *IEEE Access*, vol. 7, pp. 3360–3370, 2019, doi: 10.1109/ACCESS.2018.2888639.

[15] T. Li, Y. Gao, K. Wang, S. Guo, H. Liu, and H. Kang, "Diagnostic assessment of deep learning algorithms for diabetic retinopathy screening," *Inf. Sci.*, vol. 501, pp. 511–522, Oct. 2019, doi: 10.1016/j.ins.2019.06.011.

[16] V. Gulshan, L. Peng, M. Coram, M. C. Stumpe, D. Wu, A. Narayanaswamy, S. Venugopalan, K. Widner, T. Madams, J. Cuadros, R. Kim, R. Raman, P. C. Nelson, J. L. Mega, and D. R. Webster, "Development and validation of a deep learning algorithm for detection of diabetic retinopathy in retinal fundus photographs," *JAMA*, vol. 316, no. 22, p. 2402, Dec. 2016, doi: 10.1001/jama.2016.17216.

[17] G. T. Zago, R. V. Andreao, B. Dorizzi, and E. O. Teatini Salles, "Diabetic retinopathy detection using red lesion localization and convolutional neural networks," *Comput. Biol. Med.*, vol. 116, Jan. 2020, Art. no. 103537, doi: 10.1016/j.compbiomed.2019.103537.

[18] C. Lam, D. Yi, M. Guo, and T. Lindsey, "Automated detection of diabetic retinopathy using deep learning," *AMIA Joint Summits Transl. Sci. Proc.*, vol. 2017, pp. 147–155, 2018. [Online]. Available: http://www.ncbi.nlm.nih.gov/pubmed/29888061

[19] R. Ghosh, K. Ghosh, and S. Maitra, "Automatic detection and classification of diabetic retinopathy stages using CNN," in *Proc. 4th Int. Conf. Signal Process. Integr. Netw. (SPIN)*, Feb. 2017, pp. 550–554, doi: 10.1109/SPIN.2017.8050011.

[20] K. Xu, D. Feng, and H. Mi, "Deep convolutional neural network-based early automated detection of diabetic retinopathy using fundus image," *Molecules*, vol. 22, no. 12, p. 2054, Nov. 2017, doi: 10.3390/molecules22122054.

[21] X. Wang, Y. Lu, Y. Wang, and W.-B. Chen, "Diabetic retinopathy stage classification using convolutional neural networks," in *Proc. IEEE Int. Conf. Inf. Reuse Integr. (IRI)*, Jul. 2018, pp. 465–471, doi: 10.1109/IRI.2018.00074.

[22] H. Pratt, F. Coenen, D. M. Broadbent, S. P. Harding, and Y. Zheng, "Convolutional neural networks for diabetic retinopathy," *Procedia Comput. Sci.*, vol. 90, pp. 200–205, 2016, doi: 10.1016/j.procs.2016.07.014.

[23] R. A. Welikala, M. M. Fraz, J. Dehmeshki, A. Hoppe, V. Tah, S. Mann, T. H. Williamson, and S. A. Barman, "Genetic algorithm based feature selection combined with dual classification for the automated detection of proliferative diabetic retinopathy," *Computerized Med. Imag. Graph.*, vol. 43, pp. 64–77, Jul. 2015, doi: 10.1016/j.compmedimag.2015.03.003.

[24] J. Lachure, A. V. Deorankar, S. Lachure, S. Gupta, and R. Jadhav, "Diabetic retinopathy using morphological operations and machine learning," in *Proc. IEEE Int. Advance Comput. Conf. (IACC)*, Jun. 2015, pp. 617–622, doi: 10.1109/IADCC.2015.7154781.

[25] M. Singla, S. Soni, P. Saini, A. Chaudhary, and K. K. Shukla, "Diabetic retinopathy detection using twin support vector machines," in *Advances in Bioinformatics, Multimedia, and Electronics Circuits and Signals*. Singapore: Springer, 2020, pp. 91–104.

[26] N. Eladawi, M. Elmogy, F. Khalifa, M. Ghazal, N. Ghazi, A. Aboelfetouh, A. Riad, H. Sandhu, S. Schaal, and A. El-Baz, "Early diabetic retinopathy diagnosis based on local retinal blood vessel analysis in optical coherence tomography angiography (OCTA) images," *Med. Phys.*, vol. 45, no. 10, pp. 4582–4599, Oct. 2018, doi: 10.1002/mp.13142.

[27] T. J. Jebaseeli, C. A. D. Durai, and J. D. Peter, "Segmentation of retinal blood vessels from ophthalmologic diabetic retinopathy images," *Comput. Electr. Eng.*, vol. 73, pp. 245–258, Jan. 2019, doi: 10.1016/j.compeleceng.2018.11.024.

[28] B. B. Mandelbrot and J. A. Wheeler, "The fractal geometry of nature," *Amer. J. Phys.*, vol. 51, no. 3, pp. 286–287, Mar. 1983, doi: 10.1119/1.13295.

[29] S. Talu, C. Vladutiu, L. A. Popescu, C. A. Lupascu, S. C. Vesa, and S. D. Talu, "Fractal and lacunarity analysis of human retinal vessel arborisation in normal and amblyopic eyes," *Hum. Vet. Med.*, vol. 5, no. 2, pp. 45–51, 2013.

[30] N. Popovic, M. Lipovac, M. Radunovic, J. Ugarte, E. Isusquiza, A. Beristain, R. Moreno, N. Aranjuelo, and T. Popovic, "Fractal characterization of retinal microvascular network morphology during diabetic retinopathy progression," *Microcirculation*, vol. 26, no. 4, May 2019, Art. no. e12531, doi: 10.1111/micc.12531.

[31] M. Kostic, N. Z. Gregori, N. M. Bates, N. T. Milosevic, J. Tian, W. E. Smiddy, W.-H. Lee, G. M. Somfai, W. J. Feuer, J. C. Shiffman, A. E. Kuriyan, S. Pineda, and D. C. Buc, "Investigating the fractal dimension of the foveal microvasculature in relation to the morphology of the foveal avascular zone and to the macular circulation in patients with type 2 diabetes mellitus," *Frontiers Physiol.*, vol. 9, p. 1233, Sep. 2018, doi: 10.3389/fphys.2018.01233.

[32] N. M. Bates, J. Tian, W. E. Smiddy, W.-H. Lee, G. M. Somfai, W. J. Feuer, J. C. Shiffman, A. E. Kuriyan, N. Z. Gregori, M. Kostic, S. Pineda, and D. C. DeBuc, "Relationship between the morphology of the foveal avascular zone, retinal structure, and macular circulation in patients with diabetes mellitus," *Sci. Rep.*, vol. 8, no. 1, p. 5355, Dec. 2018, doi: 10.1038/s41598-018-23604-y.

[33] Y. Ding, W. O. C. Ward, J. Duan, D. P. Auer, P. Gowland, and L. Bai, "Retinal vasculature classification using novel multifractal features," *Phys. Med. Biol.*, vol. 60, no. 21, pp. 8365–8379, Nov. 2015, doi: 10.1088/0031-9155/60/21/8365.

[34] I. Garcia, U. Molter, and R. Scotto, "Dimension functions of cantor sets," *Proc. Amer. Math. Soc.*, vol. 135, no. 10, pp. 3151–3162, Oct. 2007, doi: 10.1090/S0002-9939-07-09019-3.

[35] C. Beck and F. Schögl, *Thermodynamics of Chaotic Systems: An Introduction*. Cambridge, U.K.: Cambridge Univ. Press, 1995.

[36] Z. W. Zhu, Z. L. Zhou, and B. G. Jia, "On the lower bound of the Hausdorff measure of the Koch curve," *Acta Mathematica Sinica, English Ser.*, vol. 19, no. 4, pp. 715–728, Oct. 2003, doi: 10.1007/s10114-003-0310-2.

[37] B. B. Mandelbrot, "A fractal's lacunarity, and how it can be tuned and measured," in *Fractals in Biology and Medicine*. Basel, Switzerland: Birkhäuser, 1994.

[38] C. R. Tolle, T. R. McJunkin, and D. J. Gorsich, "An efficient implementation of the gliding box lacunarity algorithm," *Phys. D, Nonlinear Phenomena*, vol. 237, no. 3, pp. 306–315, Mar. 2008, doi: 10.1016/j.physd.2007.09.017.

[39] J. Nalepa and M. Kawulok, "Selecting training sets for support vector machines: A review," *Artif. Intell. Rev.*, vol. 52, no. 2, pp. 857–900, Aug. 2019, doi: 10.1007/s10462-017-9611-1.

[40] M. Awad and R. Khanna, "Support vector machines for classification," in *Efficient Learning Machines*, Berkeley, CA, USA: Apress, 2015, pp. 39–66.

[41] S. Karamizadeh, S. M. Abdullah, M. Halimi, J. Shayan, and M. J. Rajabi, "Advantage and drawback of support vector machine functionality," in *Proc. Int. Conf. Comput., Commun., Control Technol. (I4CT)*, Sep. 2014, pp. 63–65, doi: 10.1109/I4CT.2014.6914146.

[42] X. Xue and X. Yang, "Seismic liquefaction potential assessed by support vector machines approaches," *Bull. Eng. Geol. Environ.*, vol. 75, no. 1, pp. 153–162, Feb. 2016, doi: 10.1007/s10064-015-0741-x.

[43] S.-G. Chem and C.-Y. Lee, "Application of a support vector machine for liquefaction assessment," *J. Mar. Sci. Technol.*, vol. 21, no. 3, pp. 318–324, 2013, doi: 10.6119/JMST-012-0518-3.

[44] P. Samui, D. Kim, and T. G. Sitharam, "Support vector machine for evaluating seismic-liquefaction potential using shear wave velocity," *J. Appl. Geophys.*, vol. 73, no. 1, pp. 8–15, Jan. 2011, doi: 10.1016/j.jappgeo.2010.10.005.

[45] J. Karthikeyan, D. Kim, B. G. Aiyer, and P. Samui, "SPT-based liquefaction potential assessment by relevance vector machine approach," *Eur. J. Environ. Civil Eng.*, vol. 17, no. 4, pp. 248–262, Apr. 2013, doi: 10.1080/19648189.2013.781546.

[46] P. Samui, "Vector machine techniques for modeling of seismic liquefaction data," *Ain Shams Eng. J.*, vol. 5, no. 2, pp. 355–360, Jun. 2014, doi: 10.1016/j.asej.2013.12.004.

[47] C. D. A. Vanitha, D. Devaraj, and M. Venkatesulu, "Gene expression data classification using support vector machine and mutual information-based gene selection," *Procedia Comput. Sci.*, vol. 47, pp. 13–21, 2015, doi: 10.1016/j.procs.2015.03.178.

[48] M. H. Afif and A.-R. Hedar, "Data classification using support vector machine integrated with scatter search method," in *Proc. Japan-Egypt Conf. Electron., Commun. Comput.*, Mar. 2012, pp. 168–172, doi: 10.1109/JEC-ECC.2012.6186977.

[49] J. Cao, M. Wang, Y. Li, and Q. Zhang, "Improved support vector machine classification algorithm based on adaptive feature weight updating in the Hadoop cluster environment," *PLoS ONE*, vol. 14, no. 4, Apr. 2019, Art. no. e0215136, doi: 10.1371/journal.pone.0215136.

[50] X. Qi, S. Silvestrov, and T. Nazir, "Data classification with support vector machine and generalized support vector machine," in *Proc. AIP Conf.*, 2017, Art. no. 020126, doi: 10.1063/1.4972718.

[51] Z. Ye, L. Ma, M. Wang, H. Chen, and W. Zhao, "Texture image classification based on support vector machine and bat algorithm," in *Proc. IEEE 8th Int. Conf. Intell. Data Acquisition Adv. Comput. Syst., Technol. Appl. (IDAACS)*, Sep. 2015, pp. 309–314, doi: 10.1109/IDAACS.2015.7340749.

[52] C. F. Navarro and C. A. Perez, "Color–texture pattern classification using global–local feature extraction, an SVM classifier, with bagging ensemble post-processing," *Appl. Sci.*, vol. 9, no. 15, p. 3130, Aug. 2019, doi: 10.3390/app9153130.

[53] K. Aida-zade, A. Xocayev, and S. Rustamov, "Speech recognition using support vector machines," in *Proc. IEEE 10th Int. Conf. Appl. Inf. Commun. Technol. (AICT)*, Oct. 2016, pp. 1–4, doi: 10.1109/ICAICT.2016.7991664.

[54] C. R. D. Souza and E. B. Pizzolato, "Sign language recognition with support vector machines and hidden conditional random fields: Going from fingerspelling to natural articulated words," Tech. Rep., 2013, pp. 84–98.

[55] J. Cervantes, F. Garcia-Lamont, L. Rodríguez-Mazahua, and A. Lopez, "A comprehensive survey on support vector machine classification: Applications, challenges and trends," *Neurocomputing*, vol. 408, pp. 189–215, Sep. 2020, doi: 10.1016/j.neucom.2019.10.118.

[56] S. Huang, N. Cai, P. P. Pacheco, S. Narrandes, Y. Wang, and W. Xu, "Applications of support vector machine (SVM) learning in cancer genomics," *Cancer Genomics Proteomics*, vol. 15, no. 1, pp. 41–51, 2018, doi: 10.21873/cgp.20063.

[57] W. Yu, T. Liu, R. Valdez, M. Gwinn, and M. J. Khoury, "Application of support vector machine modeling for prediction of common diseases: The case of diabetes and pre-diabetes," *BMC Med. Informat. Decis. Making*, vol. 10, no. 1, p. 16, Dec. 2010, doi: 10.1186/1472-6947-10-16.

[58] H. M. Muda, P. Saad, and R. M. Othman, "Remote protein homology detection and fold recognition using two-layer support vector machine classifiers," *Comput. Biol. Med.*, vol. 41, no. 8, pp. 687–699, Aug. 2011, doi: 10.1016/j.compbiomed.2011.06.004.

[59] J. Chen, B. Liu, and D. Huang, "Protein remote homology detection based on an ensemble learning approach," *BioMed Res. Int.*, vol. 2016, pp. 1–11, May 2016, doi: 10.1155/2016/5813645.

[60] Y. H. Li, J. Y. Xu, L. Tao, X. F. Li, S. Li, X. Zeng, S. Y. Chen, P. Zhang, C. Qin, C. Zhang, Z. Chen, F. Zhu, and Y. Z. Chen, "SVM-prot 2016: A Web-server for machine learning prediction of protein functional families from sequence irrespective of similarity," *PLoS ONE*, vol. 11, no. 8, Aug. 2016, Art. no. e0155290, doi: 10.1371/journal.pone.0155290.

[61] J. Xia, Z. Peng, D. Qi, H. Mu, and J. Yang, "An ensemble approach to protein fold classification by integration of template-based assignment and support vector machine classifier," *Bioinformatics*, vol. 33, pp. 863–870, Mar. 2017, doi: 10.1093/bioinformatics/btw768.
[62] X. Li, S. Wu, X. Li, H. Yuan, and D. Zhao, "Particle swarm optimization-support vector machine model for machinery fault diagnoses in high-voltage circuit breakers," *Chin. J. Mech. Eng.*, vol. 33, no. 1, p. 6, Dec. 2020, doi: 10.1186/s10033-019-0428-5.
[63] M. Ehteram, V. P. Singh, A. Ferdowsi, S. F. Mousavi, S. Farzin, H. Karami, N. S. Mohd, H. A. Afan, S. H. Lai, O. Kisi, M. A. Malek, A. N. Ahmed, and A. El-Shafie, "An improved model based on the support vector machine and cuckoo algorithm for simulating reference evapotranspiration," *PLoS ONE*, vol. 14, no. 5, May 2019, Art. no. e0217499, doi: 10.1371/journal.pone.0217499.
[64] J. Berbić, E. Ocvirk, D. Carević, and G. Loncar, "Application of neural networks and support vector machine for significant wave height prediction," *Oceanologia*, vol. 59, no. 3, pp. 331–349, Jul. 2017, doi: 10.1016/j.oceano.2017.03.007.
[65] R. P. Monteiro, M. Cerrada, D. R. Cabrera, R. V. Sánchez, and C. J. A. Bastos-Filho, "Using a support vector machine based decision stage to improve the fault diagnosis on gearboxes," *Comput. Intell. Neurosci.*, vol. 2019, pp. 1–13, Feb. 2019, doi: 10.1155/2019/1383752.
[66] T. R. Gadekallu, N. Khare, S. Bhattacharya, S. Singh, P. K. R. Maddikunta, I.-H. Ra, and M. Alazab, "Early detection of diabetic retinopathy using PCA-firefly based deep learning model," *Electronics*, vol. 9, no. 2, p. 274, Feb. 2020, doi: 10.3390/electronics9020274.
[67] N. Ramachandran, S. C. Hong, M. J. Sime, and G. A. Wilson, "Diabetic retinopathy screening using deep neural network," *Clin. Experim. Ophthalmol.*, vol. 46, no. 4, pp. 412–416, May 2018, doi: 10.1111/ceo.13056.
[68] G.-M. Lin, M.-J. Chen, C.-H. Yeh, Y.-Y. Lin, H.-Y. Kuo, M.-H. Lin, M.-C. Chen, S. D. Lin, Y. Gao, A. Ran, and C. Y. Cheung, "Transforming retinal photographs to entropy images in deep learning to improve automated detection for diabetic retinopathy," *J. Ophthalmol.*, vol. 2018, pp. 1–6, Sep. 2018, doi: 10.1155/2018/2159702.
[69] D. W. Safitri and D. Juniati, "Classification of diabetic retinopathy using fractal dimension analysis of eye fundus image," in *Proc. AIP Conf.*, 2017, Art. no. 020011, doi: 10.1063/1.4994414.

MOHAMED M. ABDELSALAM received the Ph.D. degree from Mansoura University, Egypt, in 2014.

He is currently an Assistant Professor with the Department of Computer Engineering and Control Systems, Faculty of Engineering, Mansoura University. He has several research papers in medical image analysis and expert system design and analysis. His research interests include image processing, adaptive control, artificial intelligence, expert systems, computer networks, and data mining.

M. A. ZAHRAN received the Ph.D. degree from Mansoura University, Egypt, in 2000.

He held a postdoctoral position at the University of Innsbruck, Austria, from 2006 to 2007. He is currently a Professor of theoretical physics with the Department of Physics, Faculty of Science, Mansoura University. He has authored a large number of research articles in the field of fractional dynamics and nonlinear phenomena in plasma physics published in reputed international journals. He has received several awards and honors for his academic contributions and achievement.